

Article

Design and Performance Analysis of a Composite Separator with Enhanced De-Bonding Efficiency of Gas Hydrate-Bearing Sediments

Xing Fang ¹, Yufa He ^{1,*}, Zhong Li ¹, Guorong Wang ² and Shunzuo Qiu ³

¹ State Key Laboratory of Offshore Natural Gas Hydrate, CNOOC Research Institute Co., Ltd., Beijing 100028, China; fangxing2@cnooc.com.cn (X.F.)

² Department of Mechatronic Engineering, Southwest Petroleum University, Chengdu 610500, China

³ Department of International Applied Technology, Yinbin University, Yibin 644001, China

* Correspondence: heyf@cnooc.com.cn

Featured Application: The conclusions of this study can be applied to the marine natural gas hydrate solid-fluidization mining process, specifically to the sand removal process of the in situ separator, in order to enhance downhole de-sanding efficiency, improve natural gas hydrate extraction efficiency, and reduce extraction costs.

Abstract: In the marine natural gas hydrate solid-fluidization mining process, current separation devices are insufficient in de-bonding the hydrate cementation between sand particles, affecting the hydrate collection efficiency. To address this issue, a composite separator was designed in this study that is used to restrict the axial movement of cemented particles, thereby achieving the goal of enhanced de-bonding efficiency. A combined computational fluid dynamics–discrete element method simulation method was used to verify the de-bonding performance of this composite separator on weakly cemented hydrate particles with different sizes and to study the influence of the spiral flow channel structural parameters and inlet types on the de-bonding performance.

Keywords: natural gas hydrate; structural optimization; CFD–DEM coupled analysis; gas hydrate bearing sediments; de-sand



Received: 10 March 2025

Revised: 5 May 2025

Accepted: 8 May 2025

Published: 9 May 2025

Citation: Fang, X.; He, Y.; Li, Z.; Wang, G.; Qiu, S. Design and Performance Analysis of a Composite Separator with Enhanced De-Bonding Efficiency of Gas Hydrate-Bearing Sediments. *Appl. Sci.* **2025**, *15*, 5323. <https://doi.org/10.3390/app15105323>

Copyright: © 2025 by the authors. Licensee MDPI, Basel, Switzerland. This article is an open access article distributed under the terms and conditions of the Creative Commons Attribution (CC BY) license (<https://creativecommons.org/licenses/by/4.0/>).

1. Introduction

Natural gas hydrate (NGH) is a high-quality energy source characterized as clean and green with a high energy density, abundant reserves, and extensive application prospects [1]. As a clean energy source, NGH holds significant potential for efficient energy supply to meet global demands. Its application in carbon capture and storage could mitigate climate change, promoting sustainable low-carbon development. Furthermore, NGH can facilitate seabed resource extraction, opening new opportunities for the energy industry and deep-sea technological innovation. The solid-fluidization mining process proposed by Zhou [2,3] utilizes a mechanical crushing and fluidization mining technique that maintains the reservoir's temperature and pressure conditions, thereby preventing hydrate phase transitions and enhancing safety significantly. This method has already been successfully used in the Shenhu area of the South China Sea [3–5].

The primary micro-distribution forms of natural gas hydrates were initially proposed by Ecker [6] and later revised by Jiang [7]. These forms include the load bearing type, pore filling type, and cementation type, as shown in Figure 1. These distribution forms are highly correlated with the hydrate saturation [8,9].

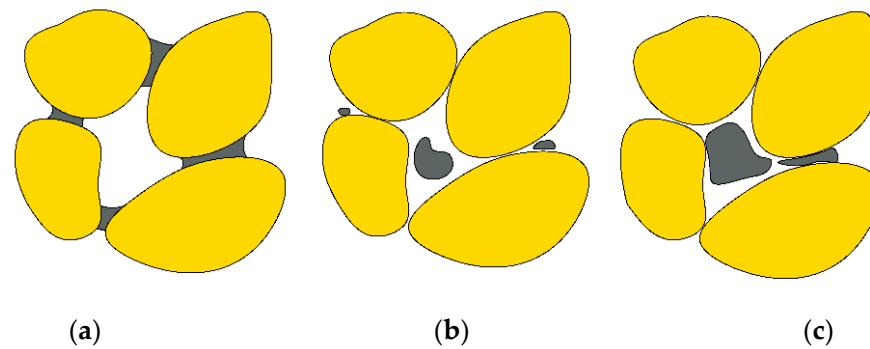


Figure 1. Three morphologies of natural gas hydrate (NGH) [7]: (a) cementation, (b) pore filling, and (c) load bearing.

Wei [1] analyzed the data from the fifth gas hydrate drilling expedition conducted by the Guangzhou Marine Geological Survey in 2018 on the northwestern slope of the South China Sea. They discovered that the hydrate saturation, based on degassing quantification, ranged from 0% to 52.9%, with an average of 14.355% [10], indicating that cementation is its primary form. According to Hu [8,9], when hydrate saturation is below 30%, the hydrate forms or partially adheres to a skeleton in the pore fluid. Therefore, during the solid-fluidization mining process, some hydrates exist as cementing bonds between sand particles, forming gas hydrate-bearing sediments (GHBSs) and returning to the mining cavity with sand from the separator underflow outlet.

Song [11] observed the characteristics of hydrate particle collision, aggregation, and rupture in a methane and water mixture in an autoclave using high-speed photography and proposed a new physical model for the aggregation of hydrate particles. Zhao [12] proposed that hydrate particle aggregation accelerates the occurrence of hydrate blockage. A low-dose antiaggregation agent is commonly used to reduce the capillary forces between hydrate particles and suspend them in the fluid to prevent the adhesion and aggregation of the particles. Bu [13] investigated the micro-distribution characteristics of the hydrate dissociation process in the South China Sea and found that breaking the sedimentary skeleton structure is the first step in hydrate dissociation. According to studies on hydrate physical properties [13], the difficulty of GHBS dissociation is closely related to the cementation state, and the destruction of the hydrate skeleton in GHBSs promotes hydrate dissociation and dispersion. Therefore, breaking the hydrate cementing bonds will promote the dissociation of weakly cemented hydrate particles and improve the hydrate collection rate.

However, in practical mining processes, mechanical crushing and jet fluidization cannot completely sever the micro-connection between the hydrate and sand [10]. Some hydrates remain attached to sand particles in the form of liquid bridges. During the downhole in situ separation process, these hydrates are discharged along with the sand from the underflow outlet, refilling to the mining cavity and reducing the overall hydrate collection efficiency, thereby increasing the difficulty of achieving commercial-scale hydrate extraction. These findings support the perspective that breaking hydrate cementing bonds to promote the dissociation of weakly cemented hydrates can enhance the efficiency of hydrate recovery.

Fang [14] investigated the feasibility of using classic hydrocyclone separators to achieve the de-bonding of weakly cemented hydrates and found that de-bonding primarily occurs in the cylindrical section of the separator. However, the de-bonding performance of classic hydrocyclone separators does not meet the requirements for commercial extraction, leading to a significant number of hydrates being refilled with sand, thus lowering the hydrate recovery rate. Since the most critical location for de-bonding in hydrocyclone separators is the cylindrical section, increasing the load on the cementing bonds in this

section and extending the residence time of particles can effectively enhance the de-bonding effect. Nevertheless, improving the de-bonding performance by adjusting the structural parameters of classic hydrocyclone separators is not cost-effective.

Wang [15,16] used a combined computational fluid dynamics–discrete element method to study the interaction behavior between hydrate particles, sediment particles, pipelines, and fluids at a pipeline constriction, revealing the mechanism of hydrate migration and deposition at the constricted section of the pipeline. Qiu [17–19] used a combination of helical and hydrocyclone separators to enhance the performance. The above results indicate that the insufficient residence time of particles constitutes the primary factor contributing to the suboptimal de-bonding performance of classic hydrocyclone separators. This issue can be effectively addressed through the implementation of a combination of helical and hydrocyclone separators, which significantly enhances the residence time of particles. Building on this, this paper proposes a new type of composite in situ separator designed with a tangential inlet to improve its de-bonding performance.

2. Background: Experimental Research

This chapter summarizes prior experimental research on the motion behavior of cemented hydrate particles in a hydrocyclone separator, as reported in [14]. These findings provide the foundation for the composite separator design and simulation studies presented in subsequent sections.

2.1. Experiment Preparation

To verify the motion behavior of cemented hydrate particles in a hydrocyclone separator, an experimental setup was constructed using substitute sample particles for testing and observation. Since the residence time of GHBS particles in a separator is very short [14], hydrate decomposition during this process was neglected in this experiment. To reduce costs, the experiment was conducted under room temperature and pressure conditions. The main components of the setup included several water tanks, a water pump, multiple flow meters, multiple valves, an acrylic hydrocyclone separator, and a high-speed camera, as described in [14].

In this experiment, spherical ceramic particles and waterproof glue were used to produce GHBS sample particles. To reduce costs, a model consisting of only two particles was created, as described in [14]. The two ceramic particles were connected by waterproof glue to simulate the formation of sand particles connected by hydrate liquid bridges. The sizes of the ceramic particles ranged from 1 to 1.1 mm, and the material specifications are shown in Table 1.

Table 1. Material parameters of substitute GHBS particles, adapted from [14].

	Spherical Ceramic Particles	Waterproof Glue
Density	2.7 g/cm ³	0.833 g/cm ³
Tensile Strength	/	0.6 MPa
Particles	1–1.1 mm	/

During the experiment, clear water was pumped into the separator, and pretreated cemented particle substitutes were injected. Most of the particle substitutes went into the underflow tank with clear water, while a few entered the overflow tank.

Flow meters were installed at multiple locations in the pipeline to monitor the working flow rate and the split ratio of the separator. Sampling ports were set up in the pipelines to monitor the separation performance of the separator. In addition, to enhance the observation effect of the high-speed camera and based on findings from the literature [10] that the

de-bonding behavior of hydrate cemented particles mainly occurs in the cylindrical section of the separator, the high-speed camera only recorded images within the cylindrical section of the separator, as reported in [14].

2.2. Results and Discussion

The result can be found in [14], which shows the rotation behaviors of cemented particles in the separator under different inlet flow rates. According to that, the theory that particles undergo rotational motion under the excitation of the hydrocyclone field was verified. It was also found that with larger inlet flow rates, the orientations of the particles during their rotational motion were more favorable for de-bonding behavior. The above conclusions confirmed the existence of the cementation particle rotation behavior in the hydrocyclone separator, and it can be used to de-bond the particles.

For more detailed conclusions, refer to the literature [14]. Only some relevant results and conclusions are listed here.

3. Composite Separator Design

3.1. Basic Structural Design

Since the de-bonding behavior of weakly cemented hydrate particles primarily occurs in the cylindrical section of a hydrocyclone separator, and the insufficient de-bonding performance of classic hydrocyclone separators is mainly due to the GHBS particles' inadequate residence time in the cylindrical section, a composite separator was designed to address this issue. To extend the residence time, the composite separator incorporated a helical flow channel within the cylindrical section of the classic hydrocyclone separator. The helical flow channel restricted the axial acceleration of the fluid and dispersed-phase particles, thereby achieving the goal of an extended residence time. In addition, the preset flow channel aided in pre-separation. As the mixed slurry entered the flow channel, its axial velocity was converted to tangential velocity, giving the slurry more time to stratify under the action of centrifugal force, thus enhancing the separation effect.

The composite cyclone separator designed in this study was based on a hydrate solid-state fluidization development process, utilizing mechanical crushing and a water jet to extract solid hydrate. Since hydrate decomposition rarely occurs downhole, the influence of gaseous hydrate formation was ignored, and only the GHBS particles and drilling fluid were considered.

The structure and working principle of the designed tangential inlet composite separator are shown in Figure 2. The mixed slurry containing hydrates, sand, and weakly cemented hydrate particles enters the composite separator through the tangential inlet. Initially, under the influence of the helical flow channel, the slurry undergoes both rotational motion around the separator main axis and axial movement, achieving pre-separation at this stage. The denser dispersed phase tends to adhere to the wall surface, while the lighter continuous phase remains closer to the center of the separator. During this phase, the weakly cemented hydrate sediment particles also experience rotational motion and de-bonding, decomposing into sand and hydrates. As the mixed slurry enters the conical section, the dispersed phase near the wall surface moves toward the underflow outlet due to axial velocity and the push from other dispersed phases, while the continuous phase is discharged from the overflow outlet.

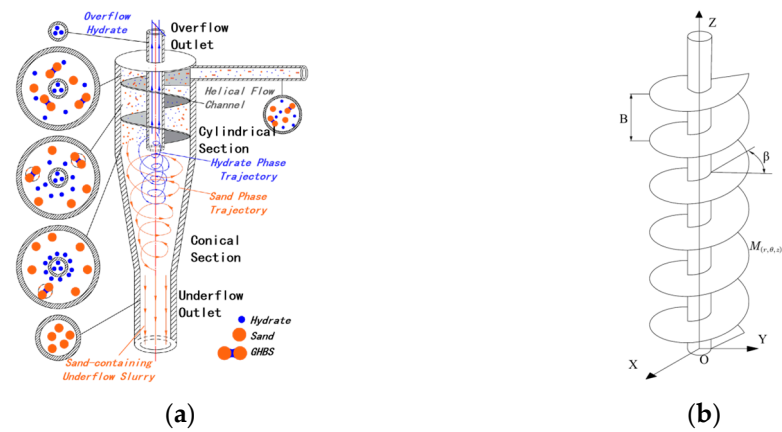


Figure 2. Structure of the composite separator. (a) Diagram of the structure of the composite separator and the internal particle motion. (b) Diagram of the helical flow channel structure in the composite separator.

3.2. Preliminarily Design of Basic Dimensions

The application site for the designed composite hydrocyclone separator was a shallow seabed natural gas hydrate solid-fluidization mining tool, which has stringent size requirements: The outer diameter of the separator body must not exceed 70 mm. Therefore, the separator body was designed with an outer diameter of 70 mm. Its basic structure is shown in Figure 3. To reduce energy consumption and mitigate the turbulence impact, a tangential inlet was chosen for the separator. The inlet size, based on the processing capacity, was selected as a rectangular inlet measuring 13 mm by 9 mm.

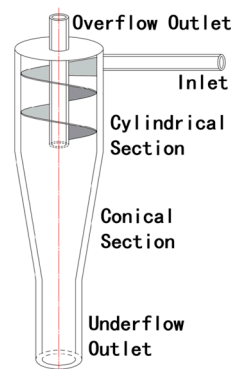


Figure 3. Structure diagram of the new composite separator.

Given that the target separation particles were sediment particles with diameters ranging from 1 to 100 μm , which belong to the fine-grain separation category, the diameter of the overflow pipe would typically be chosen to be 0.2–0.3 times the separator diameter. In this study, the preliminary design of the composite separator specified an overflow pipe diameter of 14 mm. According to findings in the literature [10], when the cylindrical section of a separator is about 120 mm, it can maintain high-stress values on the cementing bonds for a longer duration while ensuring good separation efficiency. This configuration yields the best de-bonding effect for GHBS particles in a classic hydrocyclone separator. Therefore, the cylindrical section length of the preliminarily designed composite separator was set to 120 mm.

With the length of the cylindrical section determined, the main parameter of the helical flow channel was the pitch. Since the helical flow channel converted the axial force of the fluid into tangential velocity, a smaller pitch resulted in a smaller flow channel cross-sectional area and a higher fluid tangential velocity, thereby increasing the centrifugal

force on the particles. Typically, the pitch of the helical flow channel is chosen to be 0.133–0.25 times the diameter of the separator. In this study, the pitch of the helical flow channel for the preliminarily designed composite separator was set to 20 mm.

Based on research results from the literature [10], a classic hydrocyclone separator can achieve the maximum de-bonding effect when the cone angle is 15° . At this angle, the stress value on the cementing bonds at the separator inlet is maximized, while the axial velocities of the particles do not suffer significant losses. Therefore, the preliminary design of the composite separator adopted a cone angle of 15° . The preliminarily selected structural parameters for the tangential inlet composite hydrocyclone separator are shown in Table 2.

Table 2. Main parameters of the composite in situ separator.

Structural Parameters	Value
Main Diameter (mm)	70
Pitch D_i (mm)	20
Number of Inlet Helical Turns n_i (mm)	6
Overflow Outlet Size (mm)	13×9
Length of Cylindrical Section (mm)	120
Cone Angle ($^\circ$)	15

4. Simulation Study of De-Bonding Performance of Composite In Situ Separator

4.1. Model and Mesh

For the composite separator designed in the previous section and the preliminarily designed structural parameters, a three-dimensional model was established and meshed. The results are shown in Figure 4. To achieve better simulation accuracy, the separator was meshed using hexagonal grids, and the boundary layer was delineated.

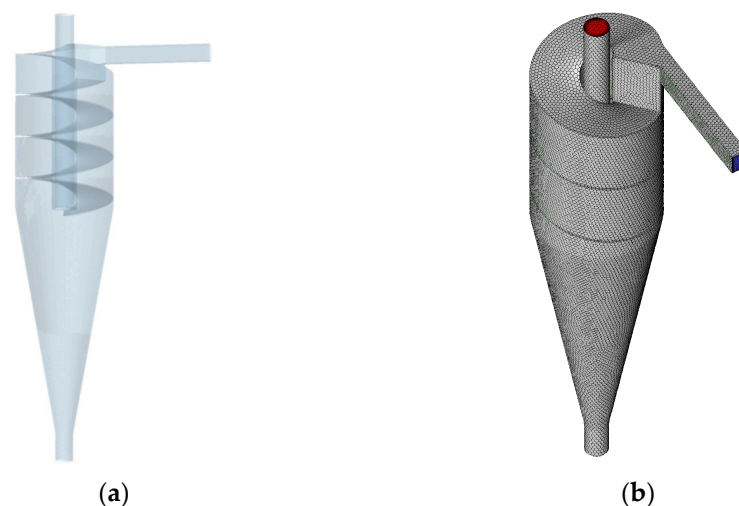


Figure 4. Model and mesh of the composite separator. (a) Three-dimensional model of composite separator. (b) Meshing result.

In addition, to conserve computational resources, mesh partitioning and independence tests were conducted for seven grid sizes; the details of the grid sizes and total numbers of grid elements are presented in Table 3. According to the results, when the grid size was not less than 1.6 mm (i.e., the number of grid elements was not less than 236,273), the reduction in grid size had a minimal impact on the simulation results (the difference was less than 5%).

Table 3. Grid sizes and total number.

Grid Sizes (mm)	1	1.2	1.4	1.6	1.7	1.8	2
Total Numbers of Grid Elements	1,796,787	1,038,531	527,571	236,273	181,439	137,605	50,431

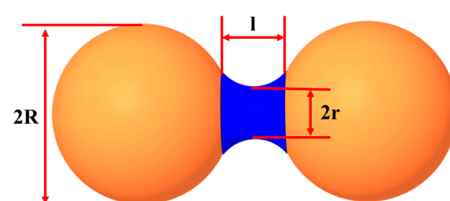
4.2. Simulation Settings

(1) Simulation Software Settings

In this study, ANSYS Fluent 19.0 was selected for simulating and analyzing the internal flow field of the separator. However, the built-in discrete element functionality of Fluent was inadequate to support the dual-sphere particle model under investigation and to extract the loads on the NGH bonds between dual-sphere particles, failing to meet the research requirements. Therefore, this study simultaneously used the particle discrete element simulation software Altair EDEM 2018 coupled with Fluent to investigate the motion behavior of hydrate particles in the hydrocyclone field.

In Fluent, the Reynolds Stress Model (seven equations), suitable for fluid rotation conditions, was chosen as the turbulence model. To couple with EDEM, the transient calculation method was used. The fluid material was seawater, with a density of 1025 kg/m^3 and a viscosity of $0.0017 \text{ Pa}\cdot\text{s}$. The inlet was set as a velocity inlet, with an equivalent velocity of 10.03 m/s corresponding to an inlet flow rate of $4 \text{ m}^3/\text{h}$. The outlet was set as a pressure outlet.

In EDEM, sand particles were modeled as two spheres, each with a diameter of 0.6 mm , and the bonding between particles was established through an API, with a length of 0.06 mm , as shown in Figure 5. A particle factory was set up at the separator inlet to inject sand particles into the separator at a rate of 1000 particles/s , with a particle velocity of 10.03 m/s . During the post-processing of the simulation results, the loads on the bonds could be extracted to analyze whether GHBS particles could achieve de-bonding. In addition, Hertz–Mindlin (no-slip) was used as the particle-to-particle contact model; the Euler model was the time integration method; the mesh size was 0.9 mm ; and the time step was $1.18 \times 10^{-6} \text{ s}$.

**Figure 5.** Weakly cemented GHBS particle model diagram.

(2) Coupling Method

In the coupling of ANSYS Fluent 19.0 and EDEM, Fluent was run independently first to allow the flow field within the separator to reach a stable state, followed by coupling with EDEM. Calculations revealed that when the simulation time was no less than 3 s , further increases in the simulation time did not significantly impact the flow field within the separator. Therefore, the pre-simulation time for Fluent was set to 3 s . A two-way coupling method was used, along with a 20-fold Fluent Drag Law Particle Scale-Up Factor. As a result, the actual particle size of the sand particles in the simulation was $30 \mu\text{m}$. The reason for using the Fluent Drag Law Particle Scale-Up Factor was that the grid size in EDEM depends on the smallest particle size. Using the real particle size would result in a

grid number no less than 1×1010 , and the Particle Scale-Up Factory could greatly reduce the computational costs.

(3) Reliability Verification

To verify the reliability of the simulation model, calculations were performed using the same particle size and five inlet flow rates as in experiments reported previously [10]. The particle linear velocity and particle trajectory distribution obtained were compared with the experimental results. The results showed that the error between the simulation and the experiment did not exceed 10%, indicating that the computational model used in this study was reliable.

(4) Simulation Scheme

The helical flow channel enhanced the de-bonding performance primarily by restricting the axial movement speed of GHBS particles, making the pitch of the helical flow channel a major variable. In addition, the particle size significantly impacted the strength of the cementing bonds and their motion behavior. Therefore, the inlet type, the pitch of the helical flow channel, and the particle size were selected as the main research factors to examine the de-bonding performance of the designed composite separator.

Given that the length of the cylindrical section was preliminarily selected as 120 mm, 7, 6, 5, 4, and 3 turns were selected, corresponding to pitches of 17.1, 20, 24, 30, and 40 mm, respectively. The particle size range was 10–50 μm , sizes for which classic hydrocyclone separators cannot efficiently achieve de-bonding. The specific simulation scheme is shown in Table 4.

Table 4. Simulation plan.

Variable	1st	2nd	3rd	4th	5th
Helical Section Pitch (mm)	17.1	20	24	30	40
Inlet Type	Tangential	Circular	Involute	Oblique	\
Particle Diameter (μm)	10	20	30	40	50

4.3. Results and Discussion

(1) Pitch

1. Axial Displacement

Figure 6 shows the relationship between the axial displacement and time for GHBS particles under different helical flow channel pitches. By comparing these results with those in the literature [10], it is evident that the addition of the helical flow channel effectively extended the residence time of GHBS particles in the cylindrical section of the separator, from approximately 0.12 s in the classic hydrocyclone separator to about 0.45 s. Although the residence times of particles in the cylindrical section were roughly the same, around 0.45 s, for different pitches, a rapid decrease in the axial velocity was observed near the exit of the helical section. According to the subsequent particle trajectory results (Figure 7), this turning point occurred because the particles' high axial velocities overcame the boundary layer effect and caused collisions with the flow channel, indicating that the total residence time of particles in the separator was not linearly related to the pitch.

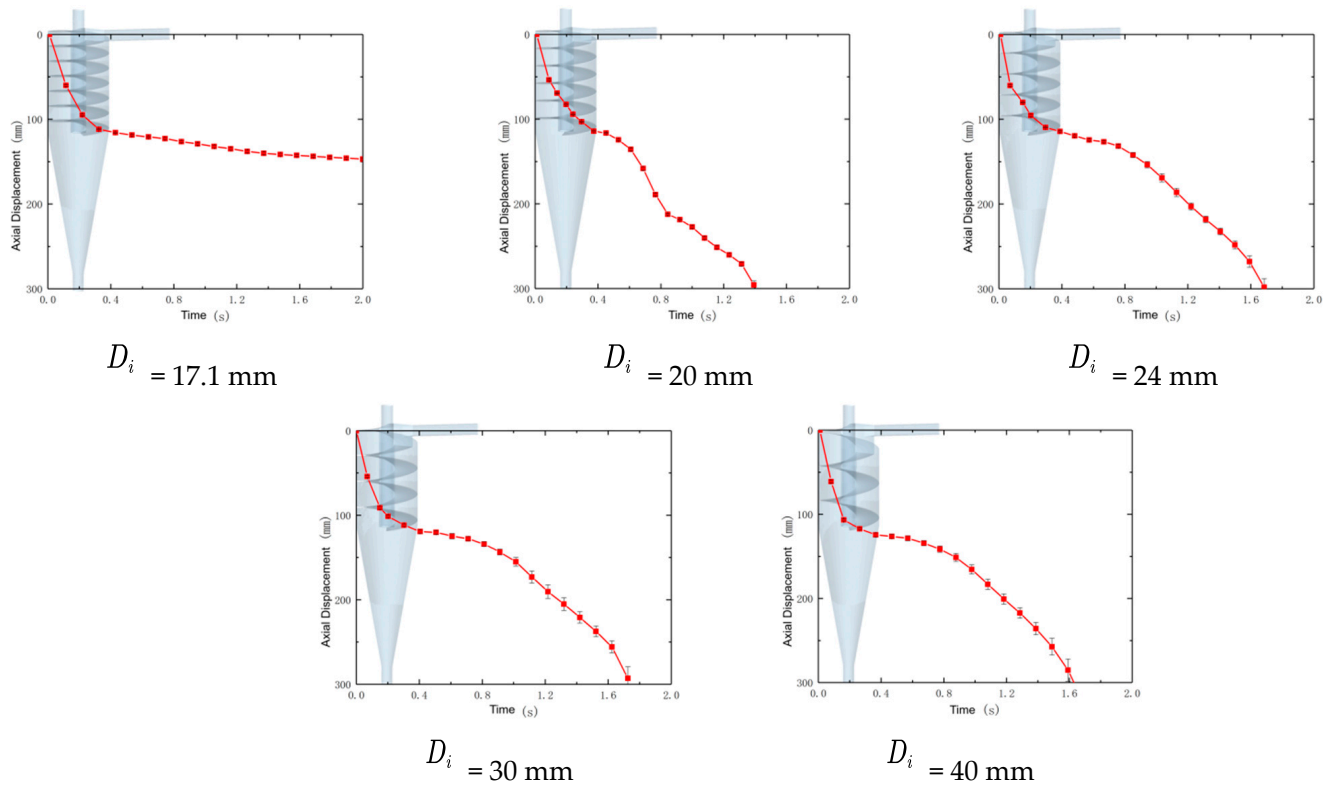


Figure 6. Relationship between axial displacement and particle residence time for different pitches.

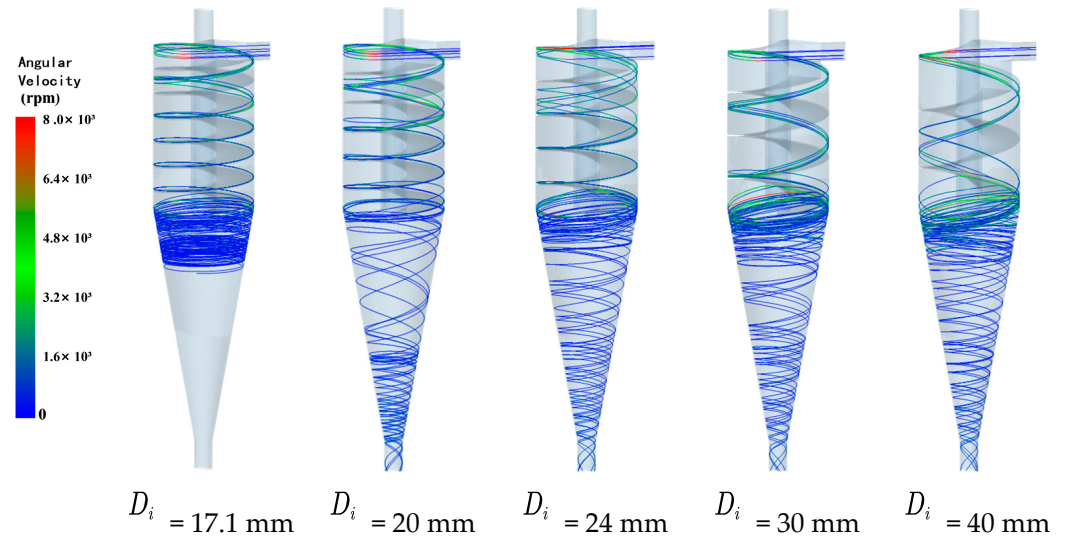


Figure 7. Particle trajectories with different pitches.

Moreover, since the helical flow channel reduced the axial velocities of GHBS particles in the cylindrical section, it also affected their axial movement in the conical section. When the pitch was 17.1 mm, the residual axial velocities of the GHBS particles upon leaving the cylindrical section were insufficient to overcome the axial separation in the conical section, preventing movement toward the underflow outlet within 2 s of the simulation.

2. Particle Trajectory

In Figure 7, it can be observed that under the influence of the helical flow channel, the GHBS particle trajectories transitioned from a dispersed state at the inlet section to moving along the flow channel, eventually aligning with the flow channel. The smaller the helical pitch, the sooner the particle trajectories aligned with the flow channel. For

instance, when the pitch was 17.1 mm, the particle trajectory aligned with the flow channel at approximately one-third of the cylindrical section, whereas when the pitch was 40 mm, most particles did not align with the flow channel before leaving the cylindrical section.

3. Cementing Bond Load

Figure 8 shows the relationship between the load on the cementing bonds of GHBS particles and the axial displacement within the separator under different helical flow channel pitches. As shown in the figure, compared with the classic hydrocyclone separator [10], the designed composite separator also exhibited a large bond load value at the inlet section for GHBS particles. This peak value was not significantly affected by the flow channel pitch, which remained at around 20 kPa across all five pitches, with a standard error of approximately 4 kPa. However, in the classic hydrocyclone separator, this maximum load appeared only at the inlet and then quickly decreased, whereas in the composite separator, the cementing bond load decreased more slowly with increasing axial displacement and showed a resurgence and a second peak toward the middle and rear sections of the cylinder.

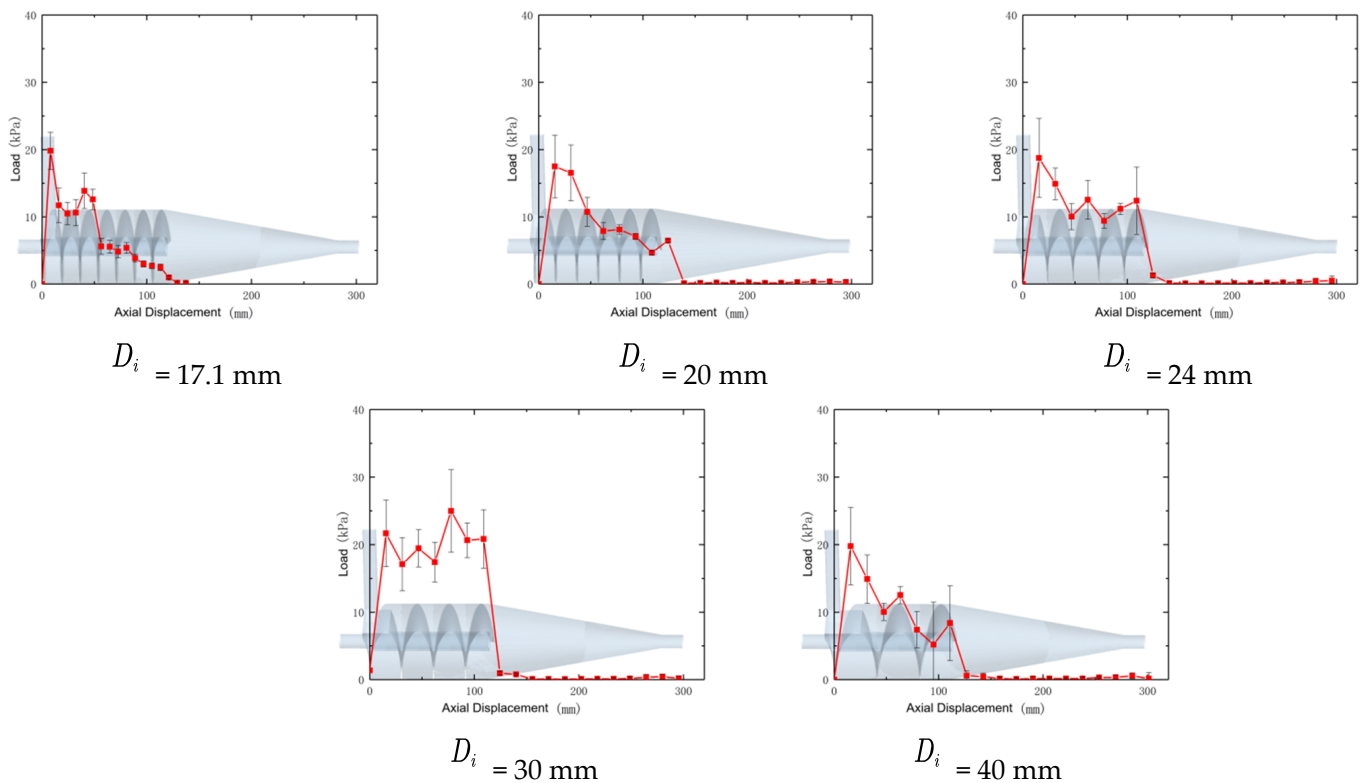


Figure 8. Relationship between the bond load and axial displacement with different pitches.

Based on Figures 6 and 7, it can be inferred that the second peak occurred due to the particles overcoming the boundary layer and colliding with the helical flow channel. This also explained why the axial position of the second peak shifted further from the inlet as the pitch increased. Among the five simulation results, the separator with a pitch of 40 mm exhibited the highest second peak value of the particle cementing bond stress, exceeding the required 21.5 kPa for de-bonding, indicating that it likely had the best de-bonding performance.

4. Pressure Gradient

The pressure gradient is an important factor affecting the load on the cementing bonds. Figure 9 shows the pressure gradient within the flow field of the composite separator for different pitches. As depicted in the figure, the smaller the pitch of the composite

separator, the greater the pressure gradient difference on the outer side. According to previous studies [17–19], a smaller pitch in the composite separator results in a higher tangential velocity of the fluid within the cylindrical section, causing the dispersed phase to experience greater centrifugal force and, thus, tending to concentrate more toward the wall surface. Consequently, the pressure gradient also increases. Therefore, in the cylindrical section of the composite separator with a smaller pitch, the pressure gradient force on the cementing bonds of the GHBS particles was also greater. Therefore, it can be concluded that when the pitch of the helical flow channel was 30 mm, the composite separator achieved the best de-bonding performance.

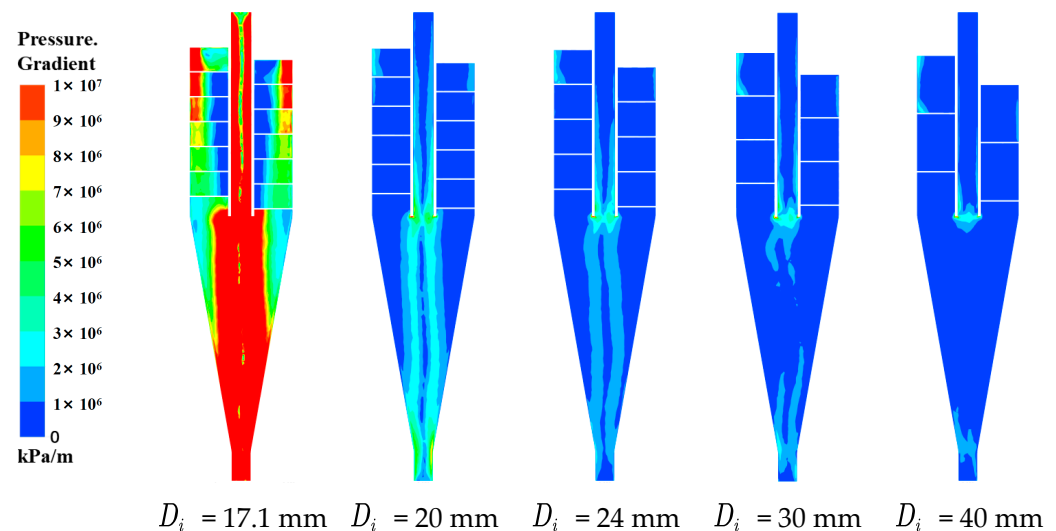


Figure 9. Pressure gradient with different pitches.

(2) Analysis of the Impact of Inlet Type on De-Bonding Performance of Composite Separator

Recently, there have been numerous studies on the impact of different inlet types on the performances of separators, which have found that inlets such as the involute type can reduce the cut size and improve the separation efficiency. To investigate whether different inlet types would affect or optimize the performance of the composite separator, three types of inlets—circular, involute, and oblique—were selected in addition to the tangential inlet for study.

1. Axial Displacement

Figure 10 shows the relationship between the axial displacement and time for GHBS particles in composite separators with different inlet types. As shown in the figure, the residence times of particles in the cylindrical section of composite separators with the four types of inlets, tangential, circular, involute, and oblique, were 0.51, 0.43, 0.33, and 0.33 s, respectively. The total residence times of particles in the composite separators with involute and oblique inlets were also shorter. Shorter residence times favor an improved working performance and throughput of the separator, but are detrimental to the de-bonding performance.

2. Particle Trajectory

Figure 11 shows the movement trajectories of GHBS particles within the composite separators with different inlet types. As shown in the figure, the main impact of different inlet types on the particle trajectories was reflected in the accelerated convergence of the particle trajectories with the flow channel. GHBS particles passing through the involute and oblique inlets had movement forms and directions that better matched the helical flow channel, leading to quicker completion of the flow in the cylindrical section and shorter

residence times. By contrast, in the composite separators with tangential and circular inlets, the particles needed to change their flow direction to adapt to the flow channel at the inlet section, resulting in longer residence times in the cylindrical section.

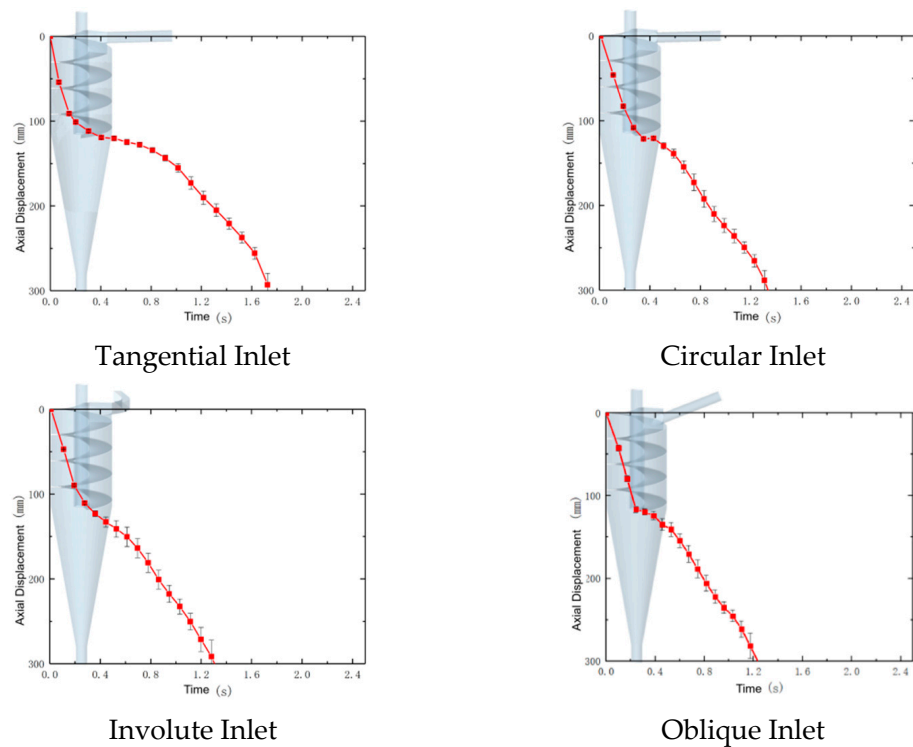


Figure 10. Relationship between axial displacement and particle residence time for different inlet types.

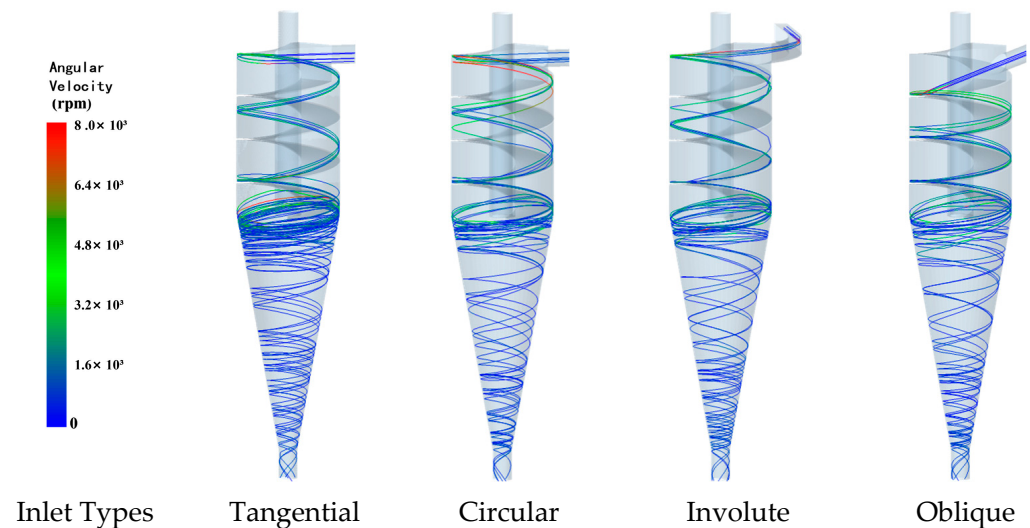


Figure 11. Particle trajectories for different inlet types.

3. Cementing Bond Load

Figure 12 shows the relationship between the load on the cementing bonds of GHBS particles and the axial displacement within the composite separators with different overflow pipe diameters. The findings are as follows.

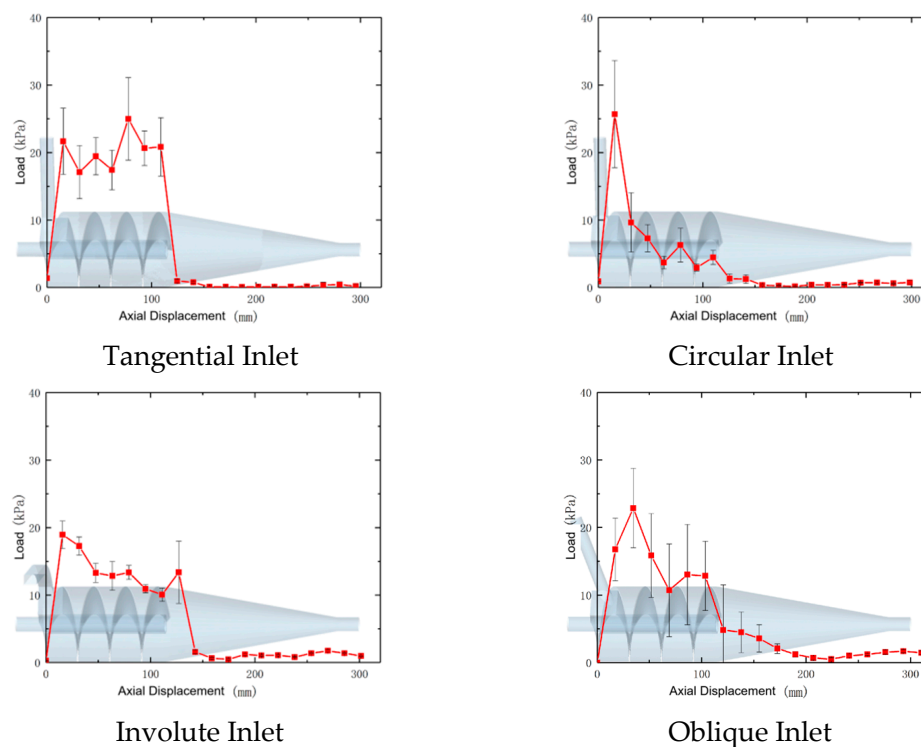


Figure 12. Relationship between the bond load and axial displacement for different inlet types.

① The tangential inlet composite separator showed the best performance among the four separators, with the highest average load value reaching about 25 kPa. It also maintained a high-stress level throughout the cylindrical section, indicating a good de-bonding effectiveness.

② The circular inlet composite separator achieved the highest cementing bond stress value of 25.7 kPa. However, high-stress values were only observed in the inlet section, with stress levels in the rest of the cylindrical section being much lower than those in other types of composite separators.

③ In the involute inlet composite separator, the cementing bond stress of the particles reached its maximum value at the inlet and then gradually decreased with increasing axial distance. Since its maximum value only reached about 19 kPa, the involute inlet composite separator could not effectively achieve de-bonding.

④ The stress values in the oblique inlet composite separator differed from those in the other three separators. Instead of reaching the maximum value immediately after entering the separator, the stress peaked at an axial displacement of about 35 mm before gradually decreasing, with a subsequent rise near the exit of the flow channel. This phenomenon occurred because the angle of the inlet was close to that of the flow channel. As a result, the fluid and particles did not immediately attain high angular velocities upon entering the separator, but gradually reached the maximum value after a certain axial displacement.

4. Pressure Gradient

Figure 13 shows the pressure gradient distributions within the composite separators with four different inlet types. As depicted, the influence of the inlet type on the pressure gradient within the separator was primarily noticeable at the inlet section, and the extent of this influence was not significant.

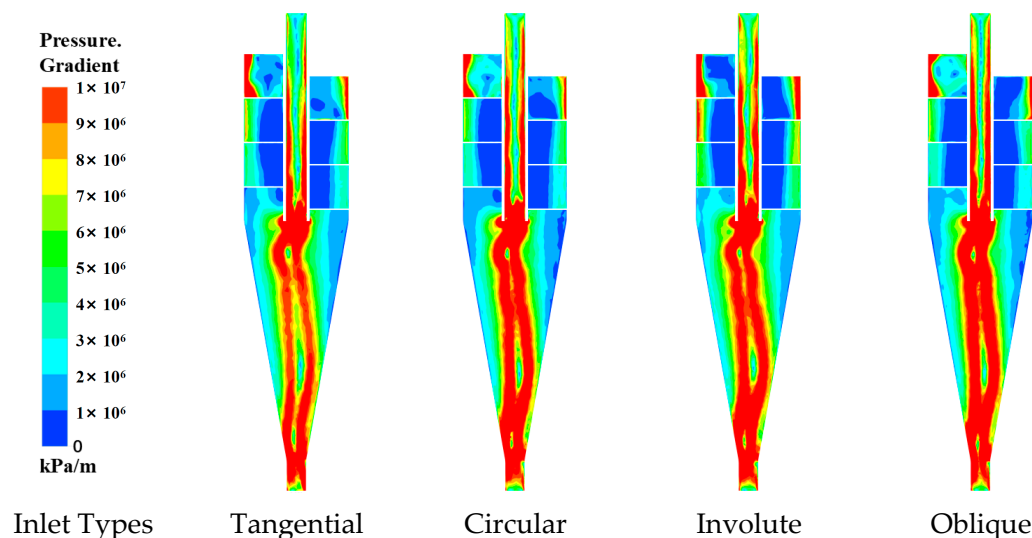


Figure 13. Pressure gradient distribution for different inlet types.

(3) Analysis of De-Bonding Performance of Composite Separator for Particles with Different Sizes

1. Axial Displacement

Figure 14 shows the relationship between the axial displacement and time for GHBS particles with different sizes within the composite separator. As shown, except for particles with diameters of $10 \mu\text{m}$, particles with various sizes had similar residence times in both the cylindrical section and the overall separator, approximately 0.4 and 1.6 s, respectively. This phenomenon significantly differed from the movement patterns of GHBS particles in a classic hydrocyclone separator. The reason for this discrepancy was that in a classic separator, larger particles, driven by their greater mass, have higher axial speeds and accelerations within the cylindrical section and encounter greater axial resistance in the conical section. In the designed composite separator, the helical flow channel caused particles with different sizes to have similar axial speeds, and the speed losses when entering the conical section were also similar, resulting in comparable residence times within the separator.

In addition, it can be observed that $10 \mu\text{m}$ particles, after moving to the middle position of the separator conical section, ceased to exhibit further axial movement and remained in the conical section. This phenomenon did not occur in the classic separator. The reason was that small-sized GHBS particles, lacking sufficient axial speed in the cylindrical section, could not overcome the resistance of the conical surface to reach the underflow outlet upon entering the conical section, leading to accumulation in the middle of the conical section. It is foreseeable that when a large number of particles accumulated in the conical section of the separator, some particles would be pushed toward the underflow outlet by the particles behind them, while others would be pushed radially, eventually crossing the zero-velocity envelope and being discharged from the overflow outlet. Therefore, it can be concluded that the composite separator reduced the separation efficiency of GHBS particles with diameters less than $10 \mu\text{m}$, thereby reducing the separator's operational performance.

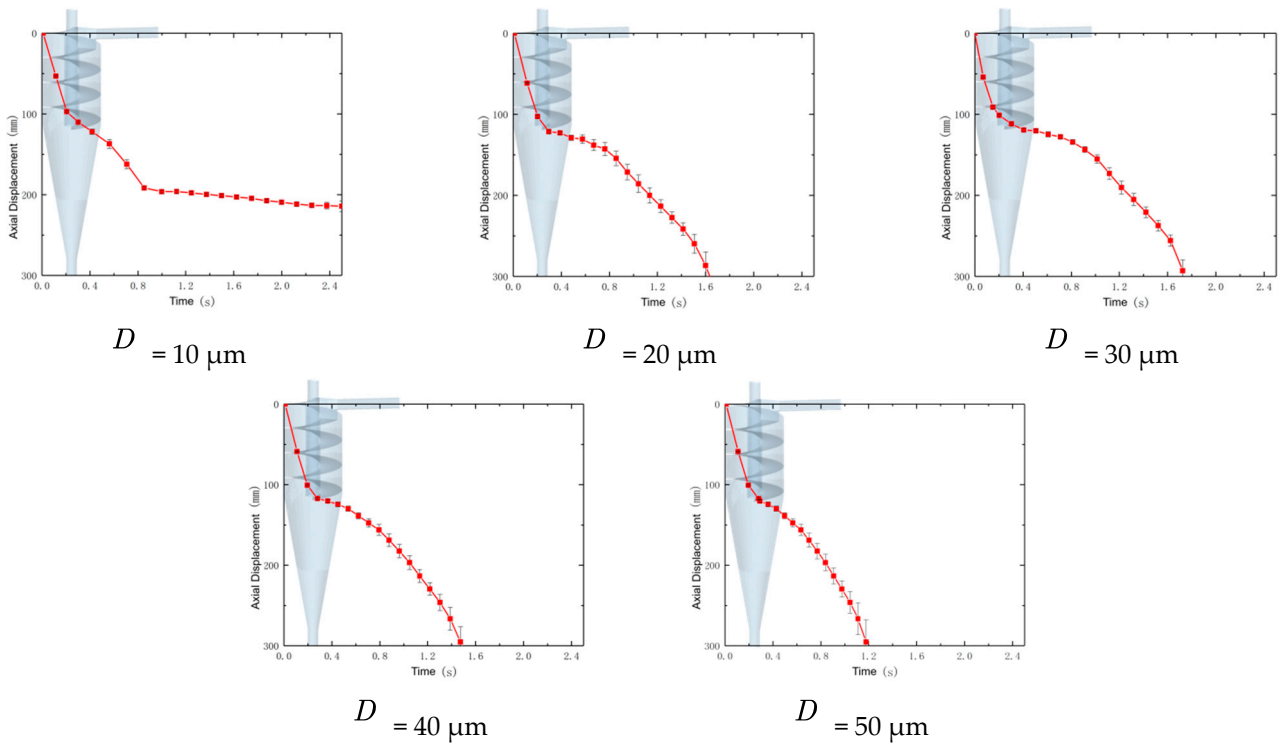


Figure 14. Relationship between axial displacement and particle residence time with different particle diameters.

2. Particle Trajectory

Figure 15 shows the trajectories of GHBS particles with different sizes within the composite separator. Particles with diameters of $10 \mu\text{m}$ did not leave the separator through the underflow outlet within 3 s, but instead accumulated in the middle of the conical section. The results indicate that when the particle diameter was not less than $20 \mu\text{m}$, there was no significant difference in the particle trajectories, only differences in the angular velocity values. Particles with diameters of $10 \mu\text{m}$ had a minimal residence time at the junction between the cylindrical and conical sections. They initially possessed high axial velocities upon entering the conical section, but experienced a rapid decrease in the axial velocity shortly thereafter, ultimately remaining in the middle of the conical section. In addition, some particles were observed to rise axially.

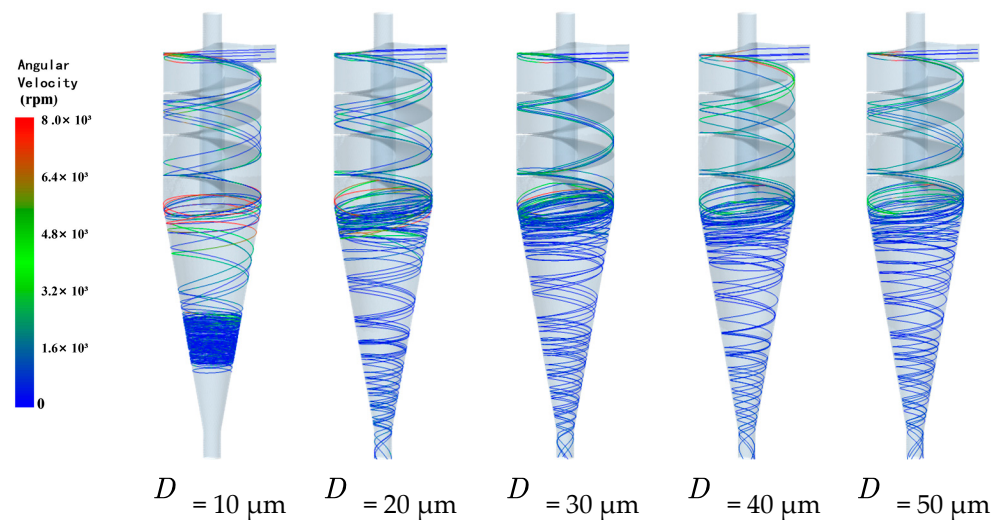


Figure 15. Particle trajectories for different particle diameters.

3. Cementing Bond Load

Figure 16 shows the relationship between the load on the cementing bonds and the axial displacement for GHBS particles with different sizes within the composite separator. The figure indicates that the cementing bond load values were proportional to the particle size. When the particle diameter was 10 μm , the cementing bond load level could not reach the 21.5 kPa required for de-bonding. When the particle diameter reached 20 μm , although the average bond load still did not reach 21.5 kPa, there was a possibility of achieving de-bonding based on the standard error. When the particle diameter was not less than 30 μm , the cementing bond load could consistently exceed the 21.5 kPa required for de-bonding. Therefore, this separator structure can effectively de-bond GHBS particles with diameters of no less than 30 μm and can partially de-bond GHBS particles with diameters of 20 μm , but cannot efficiently de-bond smaller particles.

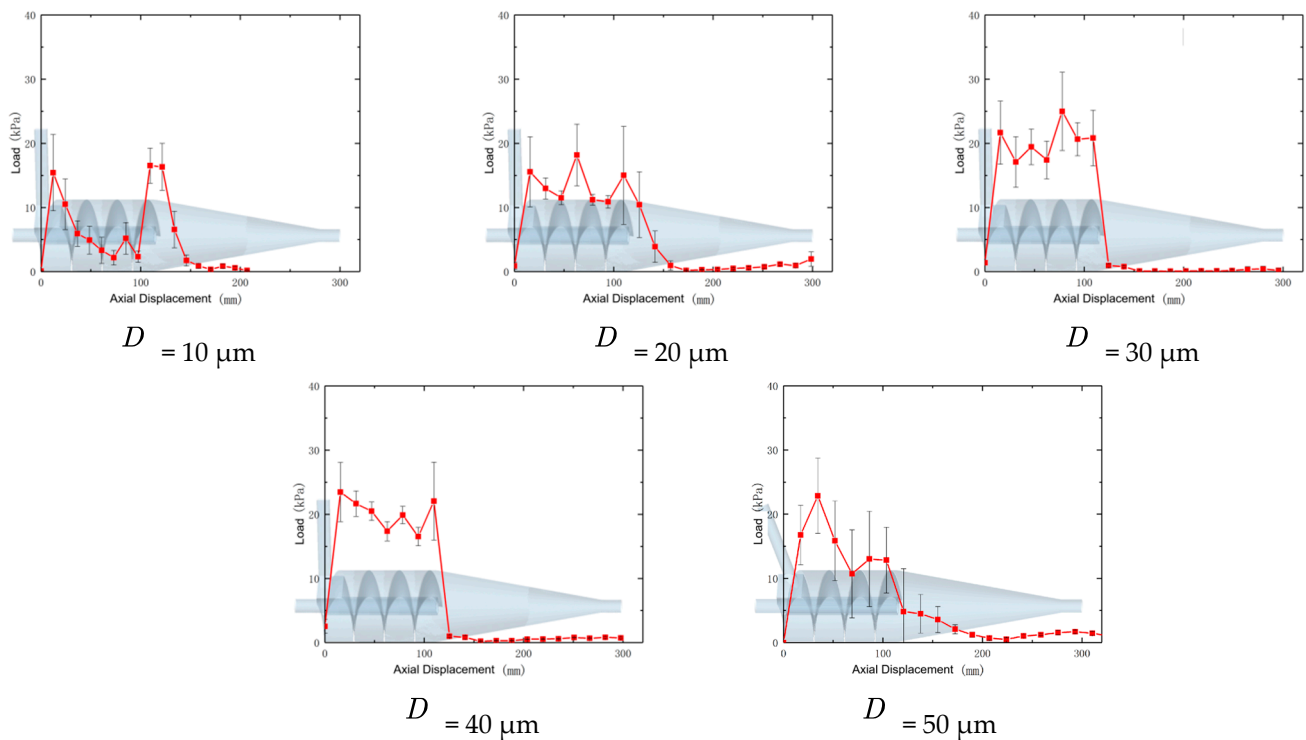


Figure 16. Relationship between the bond load and axial displacement for different particle diameters.

4. Pressure Gradient

Figure 17 shows the internal pressure gradient of the composite separator when separating particles with different sizes. It shows that when the particle diameter was not more than 30 μm , the pressure gradient within the separator increased with increasing particle size, reaching a maximum value at a particle diameter of 30 μm , but it rapidly decreased when the particle diameter exceeded 30 μm . This phenomenon occurred because at smaller particle sizes, heavier particles were more likely to gather near the wall, increasing the pressure gradient. However, when the particle size exceeded a certain range, the total mass of the dispersed phase became too large, leading to the accumulation of many large particles at the underflow outlet, affecting the flow field distribution within the separator and resulting in a decrease in the pressure gradient. Therefore, it can be concluded that the operational performance of the separator was limited when handling large quantities of large particles.

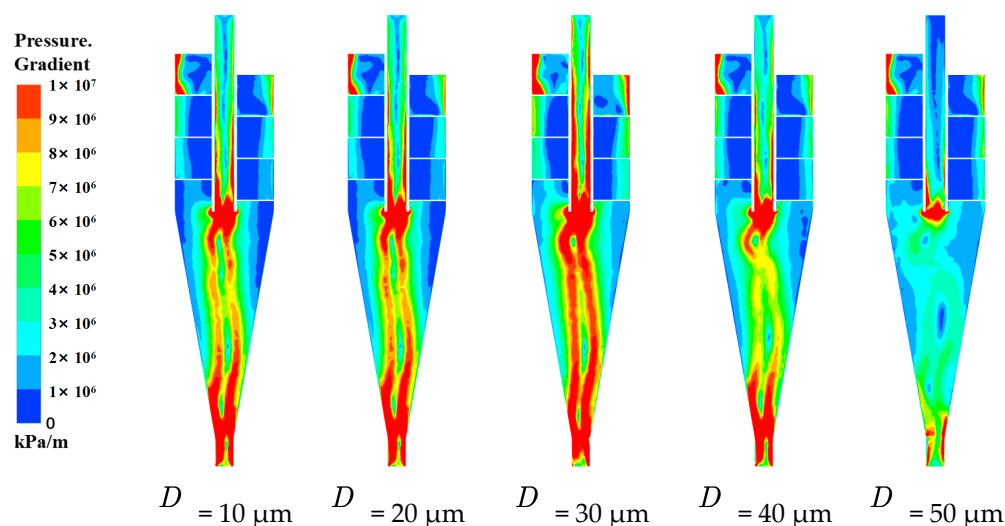


Figure 17. Pressure gradient for different particle diameters.

5. Conclusions

Based on previous research results and the theory of rotational fluids in separators, this paper proposes the use of a helical–cyclonic composite separator to improve its de-bonding performance. A preliminary structural design was created, and the de-bonding performance of the designed composite hydrocyclone separator was simulated and analyzed using a Fluent–EDEM coupling method. The effects of the pitch and inlet shape on the operational performance of the composite separator, as well as the de-bonding effectiveness for particles with different sizes, were studied. The specific conclusions were as follows.

(1) The basic structure and working principle of the composite hydrocyclone separator were determined. By adding a helical channel within the cylindrical section, the duration of the high rotational speed of GHBS particles was extended, enhancing the de-bonding performance of the separator. Particle motion theory and a separation granularity calculation method within the composite separator were established. Initial selections of the particle size and the separator structural parameters were made.

(2) The analysis of the impact of the pitch and inlet shape on the de-bonding performance of the composite separator revealed that the helical flow channel primarily changed the particle de-bonding behavior by restricting the axial displacement of fluid and particles. When the pitch was small, the particle linear velocity was high, and vice versa, but the total residence time of particles within the cylindrical section remained almost unchanged. When the composite separator used circular, involute, or oblique inlets, the internal pressure gradient increased. The cementing bond stress of particles in the inlet section with the circular inlet exceeded that with the tangential inlet, but then rapidly decreased. The total residence times of particles within the separators with these three inlet types were reduced by approximately 0.3 s.

(3) The analysis of the de-bonding performance of the composite separator for GHBS particles with different sizes showed that the value of the cementing bond stress increased with the particle size. Under the structural and operational parameters used in the simulation, the composite separator could effectively de-bond GHBS particles with diameters not less than 30 μm . For particles with diameters of 10–20 μm , only partial de-bonding could be achieved. For particles with diameters of 10 μm , de-bonding could not be achieved; these particles accumulated in the middle of the conical section and could not enter the underflow outlet, resulting in a low separation efficiency.

(4) Based on the comprehensive results of this study, it can be concluded that within the current parameter range, the structure for the designed composite separator should

have a pitch of 30 mm and use a tangential inlet. This composite separator with an inlet flow velocity of no less than 10 m/s can achieve a stable de-bonding performance for GHBS particles with diameters not less than 30 μm and partial de-bonding for particles with a diameter of 20 μm , but it cannot separate particles with diameters below 10 μm .

Author Contributions: Conceptualization, Y.H. and S.Q.; methodology, Y.H. and S.Q.; software, X.F.; validation, X.F.; formal analysis, X.F.; investigation, X.F.; resources, Y.H.; data curation, S.Q.; writing—original draft preparation, X.F.; writing—review and editing, Y.H. and G.W.; visualization, X.F.; supervision, Z.L. and G.W.; project administration, Z.L.; funding acquisition, Y.H. and Z.L. All authors have read and agreed to the published version of the manuscript.

Funding: This research was funded by the National Key Research and Development Program of China (2021YFC2800905) and the National Natural Science Foundation of China (U2244223).

Institutional Review Board Statement: Not applicable.

Informed Consent Statement: Not applicable.

Data Availability Statement: Data are available in a publicly accessible repository. The original data presented in the study are openly available in the Alibaba Cloud Drive at <https://www.alipan.com/s/Bai6gNZbUyb>, accessed on 19 March 2025.

Conflicts of Interest: Authors Xing Fang, Yufa He, and Zhong Li were employed by CNOOC Research Institute Co., Ltd. The remaining authors declare that the research was conducted in the absence of any commercial or financial relationships that could be construed as a potential conflict of interest.

Abbreviations

The following abbreviations are used in this manuscript.

NGH	Natural gas hydrate
GHBSs	Gas hydrate-bearing sediments

References

1. Wei, J.; Liang, J.; Lu, J.; Zhang, W.; He, Y. Characteristics and dynamics of gas hydrate systems in the northwestern South China Sea—Results of the fifth gas hydrate drilling expedition. *Mar. Pet. Geol.* **2019**, *110*, 287–298. [CrossRef]
2. Zhou, S.; Chen, W.; Li, Q.; Zhou, J.; Shi, H.S. Research on the solid fluidization well testing and production for shallow non-diagenetic natural gas hydrate in deep water area. *China Offshore Oil Gas* **2017**, *29*, 1–8.
3. Zhou, S.; Chen, W.; Li, Q. The green solid fluidization development principle of natural gas hydrate stored in shallow layers of deep water. *China Offshore Oil Gas* **2014**, *26*, 1–7.
4. Ye, J.; Qin, X.; Xie, W.; Lu, H.; Ma, B.; Qiu, H.; Liang, J.; Lu, J.; Kuang, Z.; Lu, C.; et al. Main progress of the second gas hydrate trial production in the South China Sea. *Geol. China* **2020**, *47*, 12. [CrossRef]
5. Ye, J.; Qin, X.; Xie, W.; Lu, H.-L.; Ma, B.-J.; Qiu, H.-J.; Liang, J.-Q.; Lu, J.-A.; Kuang, Z.-G.; Lu, C.; et al. The second natural gas hydrate production test in the South China Sea. *China Geol.* **2020**, *47*, 557–568. [CrossRef]
6. Ecker, C. *Seismic Characterization of Methane Hydrate Structures*; Stanford University: Stanford, CA, USA, 1998.
7. Jiang, M.; Zhu, F.; Liu, F.; Uti, S. A bond contact model for methane hydrate-bearing sediments with interparticle cementation. *Int. J. Numer. Anal. Methods Geomech.* **2014**, *38*, 1823–1854. [CrossRef]
8. Hu, G.W.; Ye, Y.G.; Zhang, J.; Liu, C.L.; Diao, S.B.; Wang, J.S. Acoustic properties of gas hydrate-bearing consolidated sediments and experimental testing of elastic velocity models. *J. Geophys. Res.* **2010**, *115*, B02102. [CrossRef]
9. Hu, G.W.; Li, C.F.; Ye, Y.G.; Liu, C.L.; Zhang, J.; Diao, S.B. Observation of gas hydrate distribution in sediment pore space. *Chin. J. Geophys.* **2014**, *57*, 1675–1682. [CrossRef]
10. Fang, X.; Wang, G.; Zhong, L.; Qiu, S.; Wang, D. A CFD–DEM analysis of the de-cementation behavior of weakly cemented gas hydrate-bearing sediments in a hydrocyclone separator. *Part. Sci. Technol.* **2022**, *40*, 812–823. [CrossRef]
11. Song, G.; Li, Y.; Wang, W.; Jiang, K.; Shi, Z.; Yao, S. Hydrate agglomeration modeling and pipeline hydrate slurry flow behavior simulation. *Chin. J. Chem. Eng.* **2019**, *27*, 32–43. [CrossRef]
12. Zhao, X.; Fang, Q.; Qiu, Z.; Mi, S.; Wang, Z.; Geng, Q.; Zhang, Y. Experimental investigation on hydrate anti-agglomerant for oil-free systems in the production pipe of marine natural gas hydrates. *Energy* **2022**, *242*, 1228–1237. [CrossRef]

13. Bu, Q.; Hu, G.; Liu, C.; Xing, T.; Li, C.; Meng, Q. Acoustic characteristics and micro-distribution prediction during hydrate dissociation in sediments from the South China Sea. *J. Nat. Gas Sci. Eng.* **2019**, *65*, 135–144. [[CrossRef](#)]
14. Fang, X.; Wang, G.; Zhong, L.; Wang, D.; Qiu, S.; Li, X. Analysis of weakly cemented gas hydrate-bearing sediments particles movement and de-cementation behavior in hydrocyclone separator. *Powder Technol.* **2023**, *424*, 118174. [[CrossRef](#)]
15. Wang, Z.; Li, Z.; Pei, J.; Ma, N.; Zhang, J.; Sun, B. Simulation of hydrate particles aggregation and deposition in gas-dominated flow. *SPE J.* **2024**, *29*, 1492–1509. [[CrossRef](#)]
16. Wang, Z.; Ma, N.; Zhang, J.; Pei, J.; Tong, S.; Sun, B. Numerical modeling of hydrate particle deposition in pipes with diameter reduction. *SPE J.* **2023**, *28*, 522–539. [[CrossRef](#)]
17. Qiu, S.; Wang, T.; Wang, G.; Zhong, L.; Fang, X. Effect of spiral inlet geometric parameters on the performance of hydrocyclones used for in situ desanding and natural gas hydrate recovery in the subsea. *ACS Omega* **2023**, *8*, 5426–5436. [[CrossRef](#)] [[PubMed](#)]
18. Qiu, S.; Zhong, L.; Wang, G.; Fang, X.; Yang, Y.; Liu, Q. Effect of structural parameters on the performance of axial-flow inlet hydrocyclones for in situ desanding from natural gas hydrate mixed slurry. *ACS Omega* **2023**, *8*, 28531–28542. [[CrossRef](#)] [[PubMed](#)]
19. Qiu, S.; Liu, Q.; Yang, Y.; Wang, G.; Fang, X. Structural optimization and adaptability analysis of an axial-flow inlet hydrocyclone used for in-situ desanding to purify marine hydrate slurry. *Alex. Eng. J.* **2024**, *91*, 261–272. [[CrossRef](#)]

Disclaimer/Publisher's Note: The statements, opinions and data contained in all publications are solely those of the individual author(s) and contributor(s) and not of MDPI and/or the editor(s). MDPI and/or the editor(s) disclaim responsibility for any injury to people or property resulting from any ideas, methods, instructions or products referred to in the content.